Crucial role of the Co cations on the destabilization of the ferrimagnetic alignment in Co-ferrite nanoparticles with tunable structural defects

Carlos Moya,[1,2] Arantxa Fraile Rodríguez,[1,*], Mariona Escoda-Torroella,[1] Montserrat García del Muro,[1] Sridhar R. V. Avula,[3] Cinthia Piamonteze,[3] Xavier Batlle,[1] and Amílcar Labarta.[1]

[1]Departament de Física de la Matèria Condensada, Institut de Nanociència i Nanotecnologia, Universitat de Barcelona (IN2UB), Martí i Franquès 1, Barcelona 08028, Spain.

[2]Université libre de Bruxelles (ULB), Engineering of Molecular Nanosystems, 50 Avenue F.D. Roosevelt, 1050 Bruxelles, Belgium.

[3]Swiss Light Source, Paul Scherrer Institut, CH 5232 Villigen PSI, Switzerland.

KEYWORDS (Word Style "BG_Keywords"). If you are submitting your paper to a journal that requires keywords, provide significant keywords to aid the reader in literature retrieval.

ABSTRACT: The key role of the structural defects on the magnetic properties of cobalt ferrite nanoparticles is investigated by complementary local probes: element- and site-specific X-ray magnetic circular dichroism (XMCD) combined with high resolution transmission microscopy of individual nanoparticles. A series of monodisperse samples of 8 nm nanoparticles with a tunable amount of structural defects were prepared by thermal decomposition of Fe(III) and Co(II) acetylacetonates in the presence of a variable concentration of 1,2-hexadecanediol. Particles show a partial inverse spinel structure, and their stoichiometry and cation distribution are comparable along the series. Element-specific XMCD hysteresis loops at all the cationic sites show a decrease in squareness and an increase in both the closure field and the high-field susceptibility as the nanoparticles become more structurally defective, suggesting the progressive loss of the collinear ferrimagnetism. However, the Co^{2+} cations in octahedral sites are significantly more affected by the structural defects than the rest of the cations. This is because structural defects cause local distortions of the crystal field acting on the orbital component of the cations yielding effective local anisotropy axes that cause a prevalent Co^{2+} spin canting through the spin-orbit coupling, owing to the relatively large value of the partially unquenched moment of these cations, as found by XMCD. All in all, our results emphasize the crucial role of the Co^{2+} cations on the destabilization of the collinear ferrimagnetism with the inclusion of structural defects in cobalt ferrite nanoparticles.

1. INTRODUCTION

Cobalt ferrite ($Co_xFe_{3-x}O_4$, where $0 < x \leq 1$) nanoparticles (NP) with sizes below 10 nm attract special attention in both technological and biomedical applications due to their unique physical and chemical properties.[1,2] To give a few examples, they are promising for magnetic recording due to their high coercivity at room temperature and a high Curie temperature (T_C) even for NP of few nanometers in size.[3,4] They also exhibit a comparable efficiency to iron oxide for magnetic hyperthermia due to their higher magnetic hardness and good saturation magnetization.[4–6] Furthermore, Co-ferrite NP have shown encouraging results in the detection and separation of biomolecules due to their versatile surface easily functionalized with inorganic, organic or biological compounds,[7–9] and display an enhanced magneto-optical response in combination with a noble metal.[10] From the fundamental point of view, $Co_xFe_{3-x}O_4$ NP are also interesting systems to study the occurrence of exotic magnetic phenomena in comparison with their bulk counterparts, such as spin canting due to the existence of a dead layer for NP smaller than 5 nm,[11] a reduction of the magnetic anisotropy due to the shape manipulation or an enhancement of the magnetic performance because of an improvement of the crystal quality in samples with the same particle size.[12–14] In particular, due to their spinel structure, structural defects within the NP may destabilize collinear ferrimagnetism due to the competition between the inter- and intra-sublattice superexchange interactions. Moreover, a change in the cation distribution has been shown as a source of crystal lattice distortions even for samples with a similar cation composition.[15–17] However, this phenomenon is under discussion and there are still doubts about the effect of the cation inversion on both structural and magnetic properties of these NP.[17–25]

Among the techniques used to study the effects associated with the cation distribution in these systems, synchrotron radiation-based X-ray Absorption Spectroscopy (XAS) and X-ray Magnetic Circular Dichroism (XMCD) [26] have proven to be very powerful because one can obtain local information of the electronic and magnetic

properties of NP in a wide range of temperatures and magnetic field protocols with element-, valence- and crystal site- sensitivity, both in ensembles of NP (Ref. [27] and references therein) as well as in individual NP when combined with nanoscale imaging techniques. [28]

On the other hand, to find a methodology to prepare $Co_xFe_{3-x}O_4$ NP with a great control over the structural features is of key importance. The decomposition of metal-organic precursors has shown excellent control over the particle structure by an accurate monitoring of the synthesis conditions not only in transition metal oxide particles,[29,30] but also in quantum dots,[31] metallic, and alloy NP.[32] Previously, some of us showed that the decomposition of Co(II) and Fe(III) acetylacetonates using 1-octadecene as organic solvent led to 8 nm spherical NP with narrow size distribution, homogeneous composition throughout the particle, and very similar cationic compositions.[13,14] In summary, we showed that the amount of the reagent 1,2-hexadecanediol in the reaction mixture had a great impact on the crystallinity of the particles. Without the presence of this compound, NP showed poor crystal quality and crystallite boundaries which led to a great deterioration of the magnetic properties. Hysteresis loops exhibited high magnetic irreversibility, and the coercive field and the saturation magnetization dropped sharply. In addition, zero field cooled (ZFC) curves exhibited a large reduction of the blocking temperature. In contrast, NP synthesized with increasing amounts of 1,2-hexadecanediol up to 6 mmol displayed a noticeable improvement on the structural and magnetic properties approaching those of the bulk counterpart. The actual microscopic mechanisms underlying this strong magnetic degradation are not clear yet since this is not shown to such a great extent by other ferrite NP such as the more widely studied magnetite (Fe_3O_4).

Within this framework, in this paper, we show through XAS and XMCD experiments and simulations the key role that the existence of crystalline defects in Co-ferrite NP plays on their final magnetic performance. Element-, valence- and site- specific analyses allow us to conclude that 2+ cations, in particular Co^{2+}, are much more sensitive to the presence of structural disorder within the NP than Fe^{3+} cations, showing a sharp increase on their spin canting with a smaller number of crystalline defects. Regarding Fe cations, we show that the canting takes place firstly in octahedral sites thanks to their smaller number of next-nearest neighbors in the tetrahedral sublattice, yielding a much more sensitive site to the partial substitution of tetrahedral Fe^{3+} by Co^{2+}.

On a more general note, our study highlights the crucial importance of Co^{2+} cations in the understanding of the large variability of the magnetic properties found in the literature for Co-ferrite NP with slightly different structural properties.

2. EXPERIMENTAL

2.1. Nanoparticle synthesis. Co-ferrite NP were obtained following our previous protocol described elsewhere.[13,14] Briefly, Co (II) and Fe (III) acetylacetonates were decomposed at 310 ºC in 1-octadecene using oleic acid as surfactant and with increasing concentrations of 1,2-hexadecanediol as follows: 0, 0.125, 0.25 and 0.5 mM for samples here called S1, S2, S3, and S4, respectively. Afterwards, the particles were precipitated by centrifugation, dried with compressed air, dispersed in 5 ml of hexane and stored at room temperature without further purification.

2.2. Experimental techniques. Particle size and shape were analyzed by Transmission Electron Microscopy (TEM) using a MT80-Hitachi microscope. TEM samples were prepared by placing one drop of a dilute suspension of NP onto a carbon-coated copper grid and letting it dry at room temperature. Size distributions were determined by inspection of at least 2000 NP and the resultant histograms were fitted to a log-normal function. The mean particle size (D_{TEM}) and the standard deviation (σ) were computed from these fits. The particle crystal structure was studied by the analysis of High-Resolution TEM (HRTEM) images from Titan high-base and JEOL-2100 microscopes. The crystal phase of the $Co_xFe_{3-x}O_4$ particles was identified by powder X-ray diffraction (XRD) performed in a PANalytical X'Pert PRO MPD diffractometer by using Cu Kα radiation and collecting the data within 5 and 120° for 2θ. The XRD spectra were indexed to an inverse spinel structure and the crystal size (D_{XRD}) was calculated by a Rietveld analysis using the Full Proof suite program.[33,34] The organic fraction was determined by Thermogravimetric Analysis (TGA) measurements performed using a TGA-SDTA 851e/SF1100 (Mettler Toledo) with a heating rate of 10 °C·min^{-1} from room temperature up to 800 °C in a nitrogen atmosphere. Magnetization measurements were carried out with a Quantum Design SQUID magnetometer. The values of the magnetization at 50 kOe (M_{max}) and the coercive field (H_c) were obtained from the hysteresis loops $M(H)$ recorded within ±50 kOe at 5 K and 300 K. The values of M_{max} were normalized to the magnetic content by subtracting the organic fraction estimated by TGA from the total mass of the samples. The average magnetic diameter (D_{mag}) for each sample was calculated assuming that particles at 300 K were superparamagnetic and with negligible effects due to interparticle interactions.[35] So, in this regime, $M(H)$ curves were fitted to a log-normal distribution $P(m)$ of Langevin functions $L(x)$ associated with the superparamagnetic behavior of the particles plus a linear field term caused by the lack of collinearity in the internal ferrimagnetic ordering within the particles due to the presence of crystalline defects

$$M(H,T) = M_s \frac{\int mP(m)L\left(\frac{mH}{k_BT}\right)dm}{\int mP(m)dm} + \chi_p H \qquad (1)$$

Here m is the magnetization of the crystallites that form the particles, M_s= 410 emu·cm^3 (69 emu·g^{-1}) is the saturation magnetization of bulk $Co_{0.7}Fe_{2.3}O_4$, k_B is the Boltzmann constant and χ_p is an effective paramagnetic susceptibility caused by non collinear spin contributions.[4] Since $m = M_sV_m$, where V_m is the activation magnetic volume associated with the crystallites, the distribution of V_m for each sample was computed from the fitted $P(m)$. Finally, D_{mag} was estimated from the average value of V_m assuming a spherical shape of the crystallites. ZFC magnetization curves were measured within 5–300 K with an applied magnetic field of 50 Oe. Further details of the structural and magnetic features are reported elsewhere.[13,14]

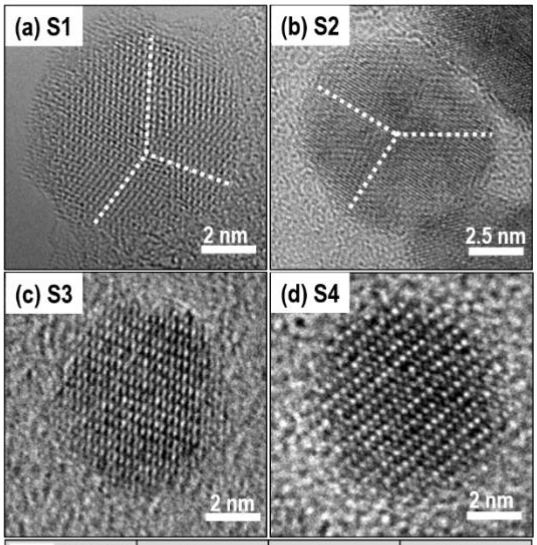

(e) Samples	D_{TEM} (nm)	D_{XRD} (nm)	D_{Mag} (nm)
S1	8.6 ± 5.2	2.1 ± 0.6	2.1 ± 0.4
S2	8.4 ± 5.0	3.2 ± 0.4	3.0 ± 0.6
S3	8.8 ± 5.3	6.2 ± 0.4	7.0 ± 0.5
S4	8.1 ± 4.9	8.0 ± 0.2	8.9 ± 0.2

Figure 1. Effect of crystallinity on the effective magnetic diameter of the samples. HRTEM images for (a) S1, (b) S2, (c) S3, (d) S4. White dashed lines in S1 and S2 indicate crystallographic domain boundaries. (e) Table summarizes the structural features for the samples: D_{TEM}, D_{XRD} , together with D_{mag} that has been obtained from magnetization measurements.

XAS and XMCD experiments around the Fe $L_{2,3}$ and Co $L_{2,3}$ edges were performed in order to gain insight into the oxidation state, cation occupancy, and atomic magnetic moment (spin and orbital moments, separately) of the Fe and Co atoms in the NP for the series of samples. Monolayered ensembles of NP were prepared by either drop casting or spin coating under a N_2 atmosphere of diluted nanoparticle suspensions onto bare SiO_x substrates. The substrates were glued with silver paste to a non-magnetic sample holder which was entered into the air-lock chamber and transferred into the cryomagnet.[36] Measurements were performed at the X-Treme beamline of the Swiss Light Source [36] with circularly polarized X-rays using a normal incidence geometry with the external magnetic field parallel to the X-ray beam. All the spectra were collected in total electron yield mode (TEY) in ultra-high vacuum conditions (~10^{-11} mbar) at a temperature of 2 K and at a magnetic field of up to ± 69 kOe at which the NP in the four samples were well saturated. TEY spectra were recorded using an on-the-fly scanning method measuring the drain current with an energy resolution better than 0.1 eV. The XMCD measurements were recorded by reversing both the circular polarization (left-/right- helicity) and the external magnetic field (± 69 kOe) to minimize measurement artifacts. The isotropic XAS were obtained by the sum of the left- and right- circular polarization data while the XMCD spectra were obtained by the difference between the left- and right- circular polarization measurements normalized to the isotropic XAS after correcting for the background. Total fluorescence yield data (TFY) were also recorded for one of the samples (S4) using a Si photodiode. The absence of detectable differences between the surface-sensitive TEY spectra and the bulk sensitive TFY XAS reveals that the electronic structure throughout the whole volume of the $Co_xFe_{3-x}O_4$ NP is the same as that of the surface.

3. STRUCTURAL AND MAGNETIC FEATURES OF CO-FERRITE NP

Figure 1 shows the main structural features together with D_{mag} obtained from magnetization measurements, for the series of samples.[13,14] All samples exhibit narrow size distributions which are very similar to each other, with a mean size D_{TEM} centered on 8 nm and a standard deviation σ of ~1 nm. HRTEM images depicted in Fig. 1a-d show round-shaped particles with interplanar distances of 2.1 (S1), 2.5 (S2 and S3) and 4.8 Å (S4) related to the atomic planes (4,0,0), (3,1,1) and (1,1,1) of the Co-ferrite, respectively.[33] Despite the good agreement in particle size and morphology, the samples show a strong dependence of the crystal quality on the concentration of 1,2-hexadecanediol in the reaction mixture. Whereas at low concentrations of 1,2-hexadecanediol, the particles exhibit defects and several crystallographic domain boundaries randomly oriented throughout the whole particle volume (Fig 1a,b), higher concentrations of this reactant lead to the formation of particles with almost no crystallographic defects (samples S3 and S4) and high structural order throughout the whole particle volume. D_{XRD} data also confirm this enhancement of the crystalline quality from samples S1 to S4, as D_{XRD} tends to D_{TEM} with increasing content of 1,2-hexadecanediol.[13,14] None of the samples show particles with defective shells, neither in composition nor in crystallographic order, as compared to their respective cores, as shown by high-angle annular dark-field (HAADF) images and energy dispersive X-ray spectroscopy (EDX) maps in Fig. S1, Supporting Information, and Supplementary Information of Ref. 14.

The magnetic properties obtained by SQUID magnetometry show a large variability, ranging from the characteristics of a frustrated cluster glass to a bulk-like ferrimagnetic behavior as the crystalline quality progressively improves. For instance, the temperature T_p corresponding to the cusp in the ZFC curve, which gives an estimation of the blocking temperature of the particles, rises monotonously along the four samples (Fig. 2a) from 150 K for S1 up to 270 K for S4. The latter compares reasonably well with previous studies of highly crystalline NP of similar sizes and stoichiometry.[13,14,37–41] However, T_p =150 K for S1 is much lower than expected for the blocking temperature of 8 nm Co-ferrite particles, suggesting that the effective magnetic volumes being actually blocked are much smaller than the size of the particles. This is a clear indication of the occurrence of more disordered magnetic arrangements in samples with poorer crystalline quality.

Moreover, $M(H)$ curves at 300 K shown in Fig. S2 in Supporting Information clearly display two different behaviors depending on the particle crystalline quality. For the most structurally defective samples, S1 and S2,

$M(H)$ show higher values of the superimposed paramagnetic susceptibility, χ_p = 0.33 ± 0.01 and 0.16 ± 0.01 emu/(g·kOe), respectively, and lower values of M_{max}. In contrast, for samples with high crystalline quality, S3 and S4, $M(H)$ curves reach saturation below 15 kOe and show much higher values of M_{max} = 60 ± 2 and 67 ± 1 emu/g, respectively.

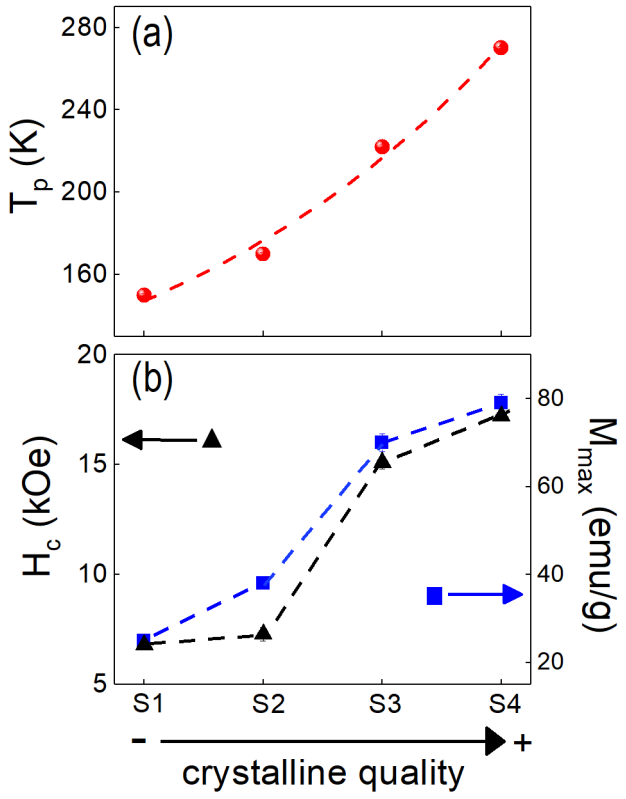

Figure 2. Main features of the magnetic characterization for the four samples. (a) Temperature T_p (red dots) corresponding to the cusp of the ZFC curves measured at 50 Oe. (b) H_c (black triangles) and M_s (blue squares) obtained from the hysteresis loops recorded at 5 K within ±50 kOe. Dashed lines are a guide to the eye.

It is worth noting that these values of M_{max} for samples S3 and S4 are only slightly lower than that of the bulk value at room temperature (69 emu·g^{-1}), which is a further evidence of their high crystalline quality. [13,14,37–41] The overall dependence of M_{max} with the samples is shown in Fig. 2b. The occurrence of a higher degree of magnetic disorder and frustration as the particle crystallinity worsens is also evident from the abrupt drop in H_c of the hysteresis loops measured at 5 K, as shown in Fig. 2b. In addition, computed values of D_{mag} (Fig. 1) found by fitting $M(H)$ curves to Eq.(1) are comparable to D_{XRD} and show an increase from 2.1 ± 0.4 to 8.9 ± 0.2 nm, in agreement with D_{TEM}, as the particles become single crystal from samples S1 to S4.[13,14]

To summarize this part, we have shown a progressive enhancement of the crystalline quality for the series of samples by the addition of increasing amounts of 1,2-hexadecanediol in the reaction mixture. Consequently, the main macroscopic magnetic features of the samples improve and show higher values of T_p in ZFC curves, M_{max} , and H_c. In addition, samples saturate at lower magnetic fields and exhibit larger D_{mag}.

4. INSIGHTS INTO THE CATIONIC MAGNETIC ORDERING BY XAS AND XMCD

The Fe $L_{2,3}$ edge XAS (not shown) and XMCD spectra shown in Fig. 3a display the usual features previously described for $CoFe_2O_4$.[17,42–44] In particular, the XMCD spectra (Fig. 3a) shows the three characteristic peaks around the Fe L_3 edge that are well known in the literature,[45] each arising predominantly from an oxidation state/site of Fe in the structure: the lowest energy, negative peak corresponds to octahedral (Oh) Fe^{2+}, the positive peak to tetrahedral (Td) Fe^{3+} and the highest, negative peak to (Oh) Fe^{3+}. The features having opposite signs reveal the antiferromagnetic coupling between the Td and the Oh sublattices. The Co $L_{2,3}$ XAS and XMCD spectra in Fig. 3b also show the typical appearance for Co-ferrite spinels containing Co^{2+} ions in both Oh and Td sites.[17,19,44,46]

A more precise analysis and understanding of the experimental XAS and XMCD data was obtained by comparison with theoretical spectra acquired from ligand field multiplet (LFM) calculations[47,48] using the CTM4XAS 5.0 program,[49] including full spin–orbit coupling, crystal field splitting, and the reduction of the *3d3d* and *2p3d* Slater integrals to account for the electronic repulsions.[49] XMCD is dependent on the magnetic moments of the Fe and Co cations in the two sublattices in the Co-ferrite structure, valence state (via the number of *d* electrons), and site symmetry (through the crystal field value).[47] The simulations define which valence state and site is responsible for each spectral peak and provide the site occupancies of each type of cation by fitting the experimental XAS and XMCD with a weighted linear combination of the LFM calculated spectra for Fe^{2+}(Oh), Fe^{3+}(Td), Fe^{3+}(Oh), Co^{2+}(Oh) and Co^{2+}(Td) for a given crystal field (Oh or Td symmetry) for each site, as hitherto done in a number of ferrite spinels.[17,19,46,50] As an example, Fig. 3 shows the fits for sample S3 of the experimental XAS and XMCD around the Fe $L_{2,3}$ edge and Co $L_{2,3}$ edge to linear combinations of the LFM calculated spectra for all the corresponding cationic sites. Details of the parameters used to perform the LFM calculations as well as the simulated spectra for all the cations are shown in Fig. S3, Supporting Information. The obtained Fe and Co cation distribution for all samples is shown in Fig. 4. Using those site occupancies, the average Fe and Co oxidation states were determined for each sample.

The orbital (m_L), spin (m_S) and total magnetic moment ($m_L + m_S$) per average Fe ion and Co ion, were determined using the XMCD sum-rule analysis [51,52] from the experimental XAS and XMCD spectra. For the $L_{2,3}$-edge spectra of transition metals, the XMCD signal is directly proportional to the atomic magnetic moment of the excited atom or ion. In our sum-rule calculations, the magnetic dipole operator, $\langle T_z \rangle$, related to the anisotropy of the spin moment within the atom, was neglected. This assumption holds when the local symmetry of the atomic sites is high,

as is the case of Co-ferrite NP with a cubic crystallographic structure, and is often used for transition metal atoms.[45,53] The total number of holes n_h per average metal ion M was estimated considering the relative distribution of cations derived from the simulations: $n_h = n_h(M^{2+})\cdot(\%M^{2+}) + n_h(M^{3+})\cdot(\%M^{3+})$, similarly to earlier works on Co-ferrites.[16,17,19] The number of holes n_h was set to 5.3 and 6.1 for Fe^{3+} and Fe^{2+}cations, respectively, and 7.21 for Co^{2+}.[17,18,54]

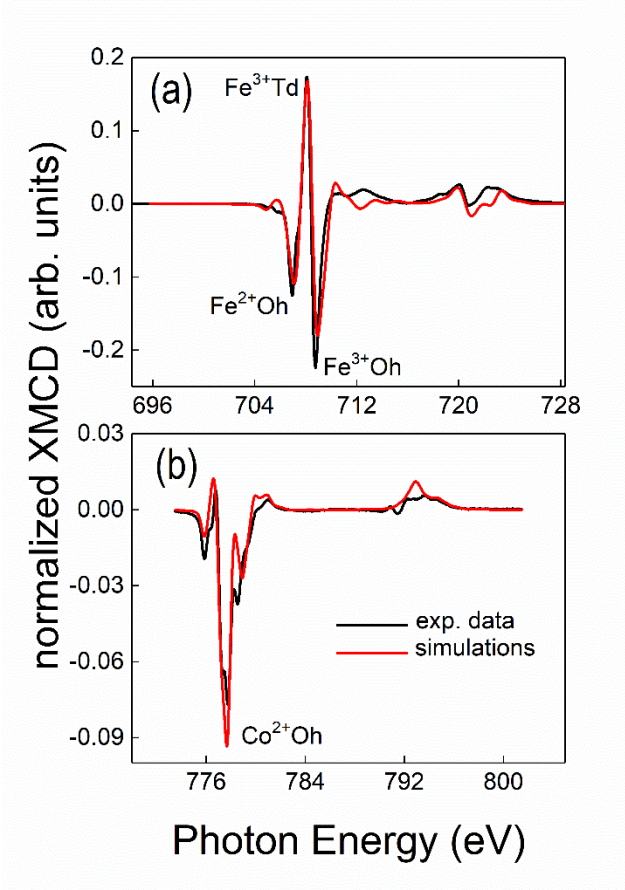

Figure 3. XMCD spectra at 2 K with H= 65 kOe recorded from sample S3. Photon energy for (a) Fe peaks: Fe^{2+} (Oh) = 706.9 eV, Fe^{3+} (Td) = 708.1 eV, Fe^{3+} (Oh) = 708.7 eV. (b) Co peak: Co^{2+} (Oh) = 777.7 eV. Black and red solid curves show experimental and LFM calculated data, respectively.

The spin and orbital contributions to the magnetic moment of Fe and Co atoms for the series of samples are displayed in Fig. 5a. The orbital contribution to the Fe moment per atom, around 0.05 μ_B, remains almost quenched for the four samples, which implies that the "spin only" model is a good approximation to account for the net moment of Fe cations. Moreover, the orbital contribution to the Co moment per atom is a bit larger, increasing from 0.15 ± 0.05 up to 0.23 ± 0.06 μ_B as the crystalline quality of the NP downgrades from samples S4 to S1.[55,56] In contrast, spin contributions are dominant to both Fe and Co moments for the four samples, showing the maximum values for the single-crystal NP in sample S4. On the one hand, the spin contribution to the Co moment per atom exhibits a monotonic decrease from 0.56 ± 0.02 to 0.28 ± 0.024 μ_B from sample S4 to S1, suggesting a remarkable and progressive effect of the structural defects on the non-collinear arrangement of the Co moments. Besides, the spin contribution to the Co moment for the most defective sample, S1, is only slightly larger than the orbital contribution, which may also be associated with a highly disordered state of the Co moments. On the other hand, the spin contribution to the Fe moments per atom remains almost constant at about 0.8 μ_B for the samples S4, S3 and S2, but experiencing a sudden drop to 0.42 ± 0.04 μ_B for S1 when the number of structural defects is large enough and the Co moments are highly misaligned. These results for the Co and Fe moments per atom as a function of the crystalline quality evidence the more robust collinear arrangement of the Fe moments as compared to Co which is more strongly affected by the inclusion of structural defects within the particles.

The net magnetic moment per formula unit (f.u.) for the four samples (black dots, Fig. 5b) was quantified from XMCD using the spin and orbital contributions from Fig. 5a and a similar average cation distribution for the four samples of $(Fe^{3+}_{0.78}Co^{2+}_{0.22})_{Td}[Fe^{2+}_{0.33}Fe^{+3}_{1.22}Co^{2+}_{0.45}]_{Oh}O_4$, as will be discussed later. Interestingly, the general trend of the net moment as a function of the crystalline quality follows quite closely that of the Fe spin contribution. There is a large increase in the net magnetic moment per f.u. from 1.41 ± 0.15 to 2.53 ± 0.39 μ_B for samples S1 and S2, respectively, while the moment remains almost constant around the latter value up to S4. This highlights the relevance of the Fe cations in stabilizing the predominant collinear contribution to the ferrimagnetic ordering in Co-ferrite NP. In Fig. 5b, the magnetic moment per f.u. estimated from the SQUID data, M_{max} is also shown for comparison. Although there are certain quantitative discrepancies between the two datasets in Fig. 5b, the general trends with the increase of structural disorder are in qualitative agreement. Interestingly, the computed value from M_{max} for the magnetic moment of S4 is 3.32 μ_B/f.u. which is quite close to the experimental value of 3.7 μ_B/f.u. for bulk $CoFe_2O_4$.[57]

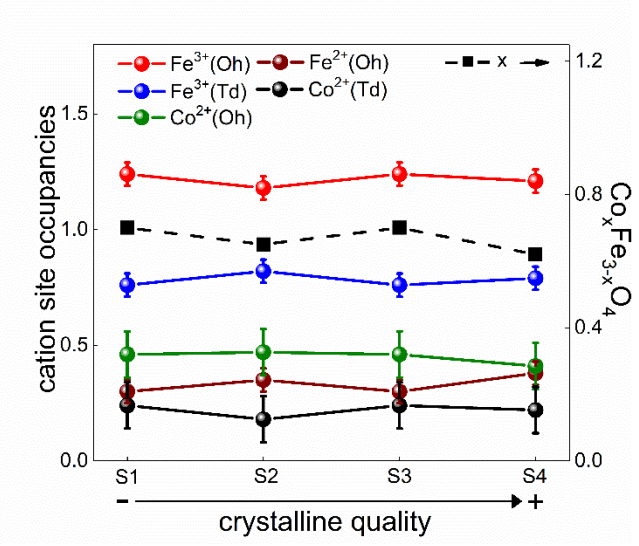

Figure 4. Cationic site occupancies (left hand-side axis) and cationic composition x (black squares, right hand-side axis) for the four samples. Dashed and solid lines are a guide to the eye.

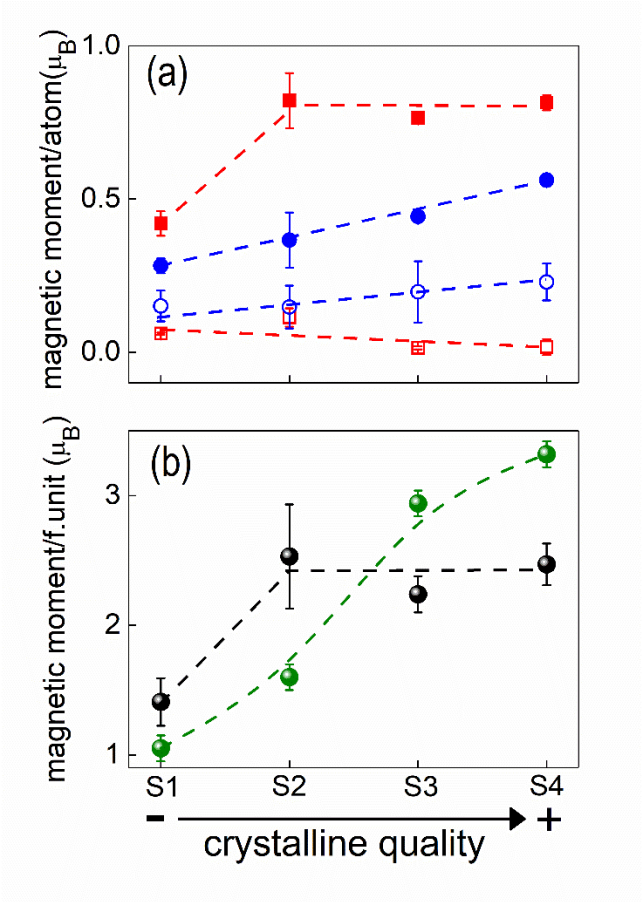

Figure 5. (a) Spin (m_S) and orbital ($m_{L)}$ contributions to the magnetic moment of every cation for the four samples obtained from XMCD data at 2K. Red solid squares and empty squares correspond to the m_S and m_L contributions to the average Fe magnetic moment per atom (m_{Fe}), respectively. Blue solid circles and empty circles correspond to m_S and m_L contributions to the average Co magnetic moment per atom (m_{Co}), respectively. (b) Net magnetic moment per formula unit (f.u.) computed from both SQUID magnetometry data at 5K, M_{max}, (green dots) and the magnetic moments per atom from XMCD in Fig. 5a (black dots). Dashed lines in both (a) and (b) are a guide to the eye.

An additional benefit of the XMCD technique is doing selective magnetometry by performing element- and site-specific hysteresis loops. By recording XMCD hysteresis loops, it is possible to evaluate the distinctive contribution of each atomic species, or ions with various valences and/or crystallographic sites to the overall magnetization reversal characteristics of the NP. To this end, the XMCD signal was measured for a fixed photon energy while varying the applied magnetic field. The hysteresis loops were collected at the Fe and Co absorption peaks from Fig. 4 corresponding to the following cations and sites: Fe^{2+} (Oh) = 706.9 eV, Fe^{3+} (Td) = 708.1 eV, Fe^{3+} (Oh) = 708.7 eV, and Co^{2+} (Oh) = 777.7 eV. Figure 6 shows the XMCD hysteresis loops measured in the TEY mode at a fixed temperature of 2 K using a magnetic field up to ± 69 kOe for the four samples. In addition, Fig. 7 shows the variation of three characteristic magnetic parameters obtained from the XMCD hysteresis loops in Fig. 6 for the four samples, namely, the superimposed high-field paramagnetic susceptibility $\chi_{p,XMCD}$ (Fig. 7a), the ratio between the remnant magnetization at zero field and the saturation magnetization $\left(M_r/M_s\right)_{XMCD}$ (Fig. 7b), and the coercive field $H_{c,XMCD}$, computed from the average of positive and negative intersections of the hysteresis branches with the field axis (Fig. 7c). As an overall picture, the XMCD hysteresis loops in Fig. 6 evidence an improvement of the magnetic order as the crystalline quality increases from samples S1 to S4. Thus, XMCD hysteresis loops for samples S1 and S2 exhibit higher $\chi_{p,XMCD}$ and lower $\left(M_r/M_s\right)_{XMCD}$ values for all the cations and sites than those for samples S3 and S4 (see Fig. 7a,b). Interestingly, these data suggest a much stronger depart from collinearity of Co^{2+} (Oh) moments with the addition of structural defects than it is found for the rest of the cations. Thereby, the hysteresis loop for Co^{2+} (Oh) in sample S3, the one with NP containing a small number of crystalline defects, is essentially the only sample which is significantly affected (Fig. 6). Moreover, the Co^{2+} (Oh) hysteresis loops for the two most defective samples, S1 and S2, resemble those of highly disordered magnetic materials, such as cluster glasses or random anisotropy systems. Note here that since XMCD is element-specific, no signal arising from the substrate is detected and thus, the XMCD hysteresis loops are much more sensitive to any slope arising from the canting of magnetic moments than SQUID magnetometry.

The increase in the canting disorder with the inclusion of structural defects of the Co^{2+} (Oh) moments is further confirmed by comparing the monotonic increasing and decreasing trends exhibited by $\chi_{p,XMCD}$ and $\left(M_r/M_s\right)_{XMCD}$, respectively, for this cation with the more staggered behavior shown by the three Fe cations. Thus, only in samples with a relatively large number of structural defects (S1 and S2) do the Fe moments seem to be significantly affected, being the Fe^{2+} (Oh) moments the ones showing the largest degradation of their magnetic features (Fig. 6). The latter is manifested by both the earlier and sustained deviation from the squareness in S1 of the Fe^{2+}(Oh) loops compared to the other Fe cations (Fig. 6) as well as by the largest deviation of the $H_{c,XMCD}$ value of Fe^{2+}(Oh) from that of the other Fe cations shown in Fig. 7c (most notably observed for S2). The reason for the stronger sensitivity of the Fe^{2+}(Oh) cations to the amount of structural defects may be a dragging effect of the Co^{2+} (Oh) moments over the Fe^{2+} (Oh) ones through the strong ferromagnetic exchange coupling existing among the 2+ cations in Oh sites. [58,59]

The overall trend exhibited by $H_{c,XMCD}$ for the four samples (Fig. 7c) is also in qualitative agreement with the former discussion but with the onset of a significant reduction of $H_{c,XMCD}$ for both Fe and Co cations corresponding to samples with a greater number of structural defects than in the cases of $\chi_{p,XMCD}$ and $\left(M_r/M_s\right)_{XMCD}$. This may be because the crystalline defects act as anchoring centers for the reversal of the individual particle magnetization, increasing, in turn, the effective coercive field of the ensemble of NP when the magnetic disorder is still small. However, as the spin alignment

departs from collinearity, the magnetic correlation among the spins in

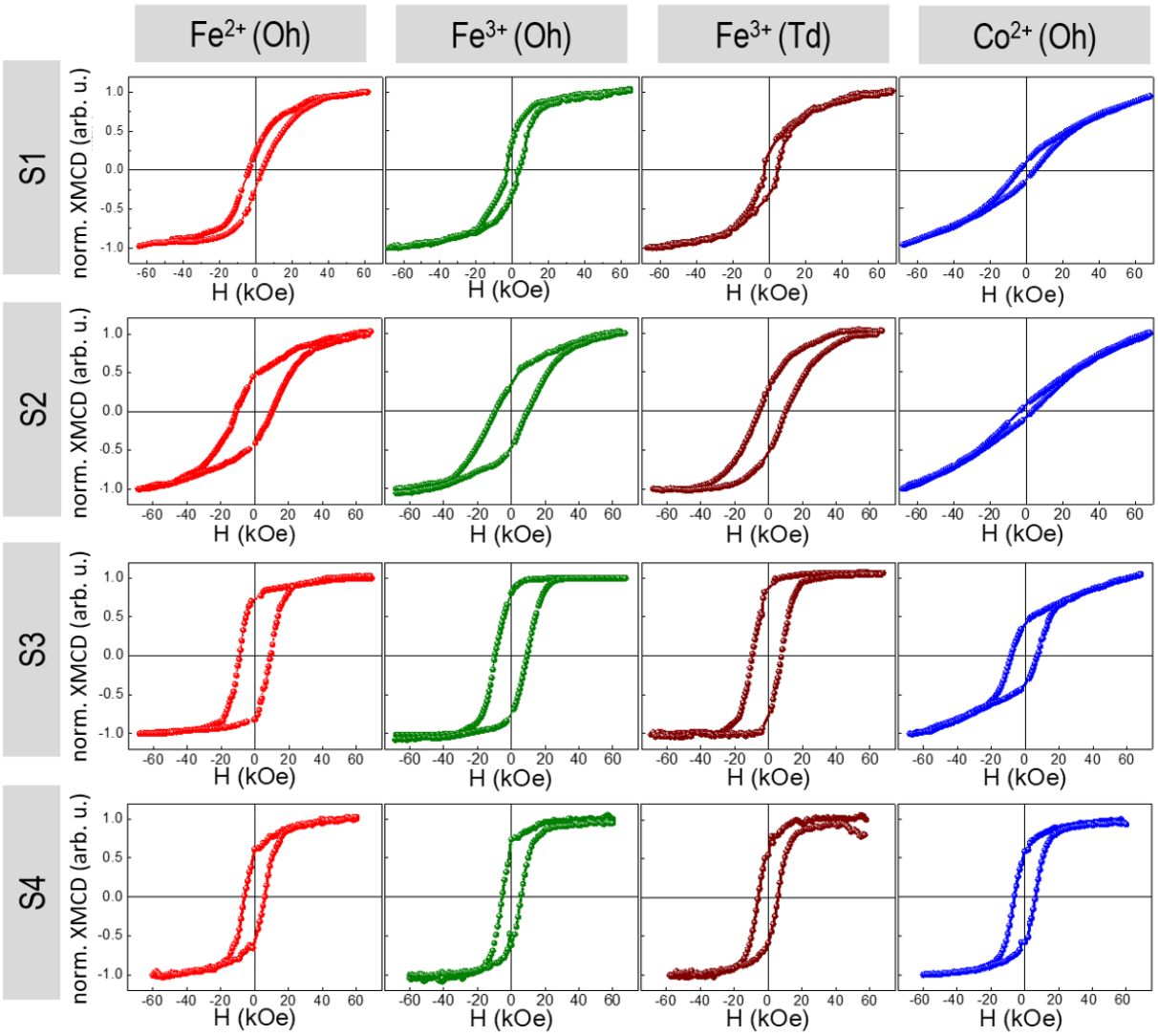

Figure 6. XMCD hysteresis loops measured at 2 K within ± 69 kOe for the four samples for the following cationic sites: Fe^{2+} (Oh), Fe^{3+} (Oh), Fe^{3+} (Td) and Co^{2+} (Oh), plotted as red, green, brown and blue curves, respectively. Note that hysteresis loops corresponding to cations in Td sites have been reversed along the magnetization axis to compare with the Oh ones.

the individual NP decreases. Therefore, when the magnetic disorder is high enough, the coercive field starts to drop. Anyhow, $H_{c,XMCD}$ for Co^{2+} (Oh) is already much smaller than those values for Fe cations in sample S2, which is a clear proof of the abrupt start of a highly non-collinear arrangement of the Co cations as the crystalline defects rise in the NP. Finally, it should be pointed out that $H_{c,XMCD}$ for sample S4 is smaller than that expected for bulk Co-ferrite, and it even looks like a bit anomalous when compared with that of sample S3. The slightly different trend found for $H_{c,XMCD}$ in sample S4 could be owed to two facts. First, sample S4 shows the greatest deviations in the formula stoichiometry, especially for the Co content and the cationic site occupancies. Second, the XMCD data for sample S4 were collected in a different set of measurements. Nevertheless, its overall magnetic properties, apart from $H_{c,XMCD}$, agree well with the general trends found in the other three samples.

Finally, for sample S4, XMCD hysteresis loops using the TFY mode were also recorded (Fig. S4, Supporting Information). The absence of detectable differences between the surface-sensitive TEY loops and the bulk sensitive TFY loops for all the cationic sites indicates that the above discussed results are representative of the whole nanoparticle volume, not only of its surface.

5. DISCUSSION

The Co-ferrite NP synthesized in this work by thermal decomposition of organic precursors have around 0.62-0.7 Co atoms/f.u. (see Fig. 4) so they have an excess of 0.38-0.3 Fe per f.u. with respect to the stoichiometric Co-ferrite. This is likely due to the small differences in the decomposition-temperature profiles of Co(II) and Fe(III) acetylacetonates

that yield an [Fe]:[Co] cationic ratio greater than 2 during the particle nucleation stage at the reaction temperature of 310 °C. This kind of non-stoichiometric Co-

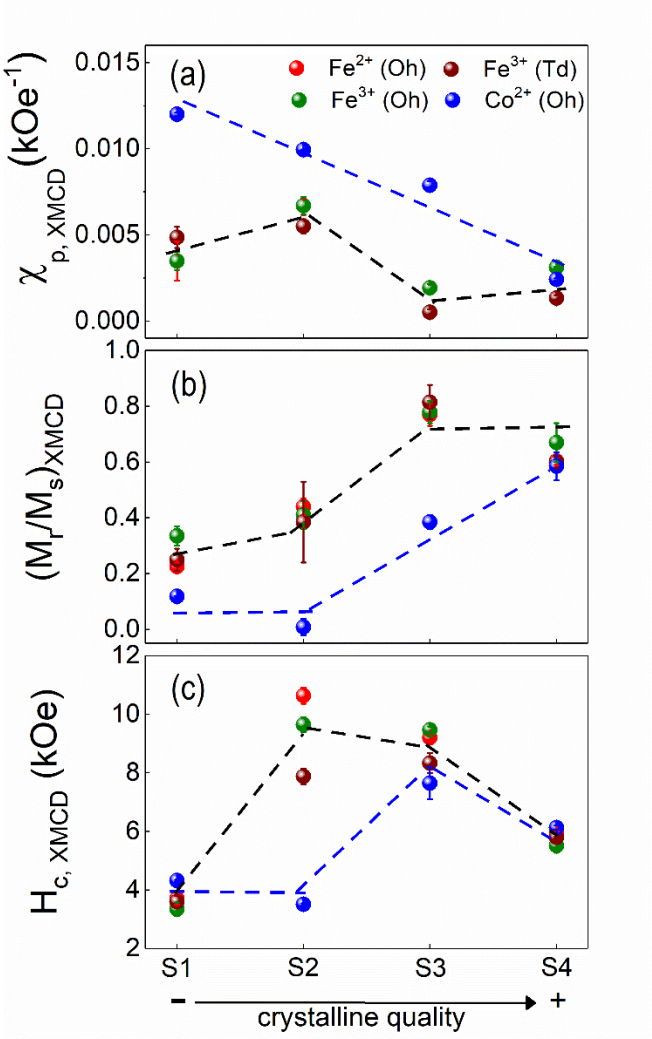

Figure 7. Magnetic parameters for the series of samples found from the analysis of XMCD hysteresis loops for Fe^{2+} (Oh), Fe^{3+} (Oh), Fe^{3+} (Td) and Co^{2+}(Oh) cations and sites. (a) High-field susceptibility $\chi_{p,XMCD}$ was computed by linear fitting of the magnetization in the high field region from 30 and 60 kOe. (b) Ratio between the remnant and the saturation magnetizations. $\left({}^{M_r}/_{M_s}\right)_{XMCD}$ ratio was found dividing the remnant and saturation magnetizations determined at zero and maximum magnetic field, respectively. (c) Coercive field. $H_{c,XMCD}$ was computed from the average of positive and negative intersections of the hysteresis branches with the field axis. Errors are indicated by the scale bars. Dashed lines are a guide to the eye.

ferrite NP with a partial substitution of Co^{2+} by Fe^{2+} are commonly obtained by thermal decomposition methods.[3,20,60] In our case, we chose preparing samples of monodisperse Co-ferrite NP of the same size with a good monitoring of their crystalline quality over getting the perfect $CoFe_2O_4$ stoichiometry, provided that the compositions and cation distributions were similar for all samples, in order to enable the comparison of their magnetic properties as a function of the number of structural defects. In addition, the actual crystal structure of our samples is not that of a fully inverse spinel ferrite since there is a partial occupation within 0.18-0.24 Co^{2+}/f.u. of the Td sites (Fig. 4). We note that values within 0.02 and 0.24 were reported even for stoichiometric $CoFe_2O_4$ depending on the temperature profile followed during the preparation method.[17,61–63] From these results, 0.67 Co^{2+}/f.u. and 0.22 Co^{2+}(Td)/f.u. can be taken as mean values for the four samples, yielding an average cation distribution of $(Fe^{3+}_{0.78}Co^{2+}_{0.22})_{Td}$ $[Fe^{2+}_{0.33}Fe^{+3}_{1.22}Co^{2+}_{0.45}]_{Oh}$ O_4. Should we now assume spin-only contributions to the cationic moments, with 5, 4, and 3 μ_B for Fe^{3+}, Fe^{2+}, and Co^{2+}, respectively, and collinear ferrimagnetic alignments of the spins in the two sublattices, the computed value for the net magnetic moment will be 4.21 μ_B/f.u. This value is much larger than any of those in the two sets of the corresponding experimental determinations shown in Fig. 5b, even for the samples with a smaller number of structural defects such as S3 and S4 (the highest experimental value being 3.32 μ_B/f.u. from M_{max} for S4). The reduced magnetic moment per f.u. with respect to the expected value for a perfect ferrimagnetic alignment may be caused by the existence of spin canting within one or both of the magnetic sublattices.[63,64] The partial cationic inversion and the competition between inter- and intra-sublattice interactions may be behind this moment reduction in samples without structural defects. In spinel ferrites the ferrimagnetic alignment is stabilized by the strong antiferromagnetic Fe^{3+}(Td)-O^{2-}-Fe^{3+}(Oh) superexchange interactions and intra-sublattice interactions are magnetically frustrated (see Fig. 8).[65] Taking into account that Oh sites have 6 next-nearest neighbors in the Td-sublattice, but Td sites have twice next-nearest neighbors in the Oh-sublattice, Fe^{3+}(Oh) moments are expected to be most affected by the partial substitution of Fe^{3+} by Co^{2+} in the Td-sublattice, since the canting takes place firstly in the sites with the smaller number of next-nearest neighbors in the other sublattice. Thus, the existence of about 0.22 Co^{2+}/f.u. in Td sites reduces the effective superexchange interaction acting on Fe^{3+}(Oh) sites in a factor around 0.68±0.04 since the Co^{2+}(Td)-O^{2-}-Fe^{3+}(Oh)

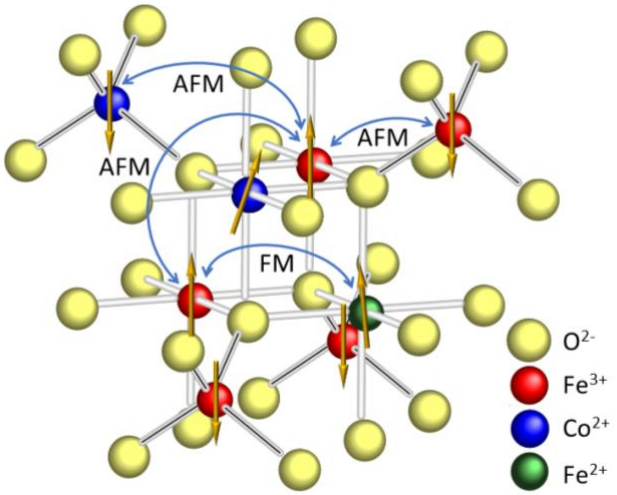

Figure 8. Schematic representation of the orientation of the net magnetic moments for the different cations and sites in the two ferrimagnetic sublattices. Yellow spheres represent oxygen atoms. Red, blue, and green spheres correspond to Fe^{3+}, Co^{2+}, and Fe^{2+} cations, respectively. The antiferromagnetic (AFM) or ferromagnetic (FM) character of the expected exchange interactions among the cations in the two sublattices is indicated next to the double-headed blue arrows connecting two sites.

interaction is weaker than Fe^{3+}(Td)-O^{2-}-Fe^{3+}(Oh) one.[64] This may result in local modifications of the prevalent ferrimagnetic arrangement of the Fe^{3+} moments that are mediated by the competition with the antiferromagnetic Fe^{3+}(Oh)-O^{2-}-Fe^{3+}(Oh) intra-sublattice superexchange interactions (see Fig. 8).[65] Then, if the amount of Co^{2+}(Td) next-nearest neighbors of an Fe^{3+}(Oh) cation is large enough, the energy balance between inter-sublattice interactions and the antiferromagnetic Fe^{3+}(Oh)-O^{2-}-Fe^{3+}(Oh) interactions will favor the canting of its moment. Therefore, assuming that the canting occurs only in the Oh-sublattice and taking the former spin-only values of the three cationic moments, it is straightforward computing that the Fe^{3+}(Oh) moment must be reduced by 15% in order to recover the experimental value of 3.32 μ_B/f.u. for the net magnetic moment of the molecule. Of course, this is just a rough estimation because some of the Fe^{2+}(Oh) and Co^{2+}(Oh) which are next-nearest neighbors of a canted Fe^{3+}(Oh) spin could be also canted. Besides, canting of the Fe^{3+} moments may also take place in the Td-sublattice.[63] Nevertheless, a simple calculation of the likelihood that an Fe^{3+}(Oh) cation has n Co^{2+}(Td) next-nearest neighbors allows us to get an estimation of a factor $J(n)$ of reduction in the effective superexchange interaction acting on Fe^{3+}(Oh) sites for the different surroundings in the Td-sublattice as

$$J(n) = \frac{1}{6}\binom{6}{n} q^n (1-q)^{6-n}(6 - n + n \cdot 0.68) \qquad (2)$$

with $q = 0.22$ being the Co^{2+}(Td)/f.u. and $J(n) \leq 1$. The values of n, $J(n)$ computed with Eq. (2), and the corresponding probabilities $p(n)$ for each surrounding are: 0, 1, 0.23; 1, 0.95, 0.38; 2, 0.89, 0.27; 3, 0.84, 0.10; 4, 0.79, 0.02; respectively (for $n > 4$ the probability is very low). Then, around 39% of the Fe^{3+}(Oh) sites have 2 or more Co^{2+}(Td) next-nearest neighbors and feel an inter-sublattice interaction which is less than 90% of that in the perfectly inverse Co-ferrite spinel. Consequently, the reduction in the net magnetic moment in the sample without structural defects (S4) and, in particular, the decrease of about 15% in the Fe^{3+}(Oh) moment needed to recover the experimental value could be explained in terms of the existence of some canting within the Fe^{3+}(Oh) cations.

When the structural defects increase within the particles (samples S3 to S1), there is another cause of moment reduction: the strain associated with the structural defects giving rise to local directions of the anisotropy that tilt the cationic moments out of the ferrimagnetic axis via the spin-orbit coupling. This canting is more prevalent in the Co^{2+}(Oh) cations due to the relatively large orbital moment, as determined by XMCD (Fig. 5). Consequently, the Co^{+2}(Oh) moments are those firstly canted with the inclusion of structural defects in the NP, as shown by the XMCD hysteresis loops (Fig. 6, blue curves). This is particularly manifested by the large superimposed high-field susceptibility, even for the sample S3, containing only a small number of structural defects. Fe^{2+}(Oh) are the next affected moments by the structural disorder, although to a much lesser extent than Co^{+2}(Oh) moments since they have a smaller orbital moment (Fig. 5). Thus, Fe^{2+}(Oh) hysteresis loops do not show significant modifications until sample S2. Interestingly, Fe^{3+}(Oh) moments start to be canted before Fe^{3+}(Td) moments do, likely because of the dragging effect via the superexchange interactions and double-exchange interactions with the already canted Co^{2+}(Oh) and Fe^{2+}(Oh) moments, respectively (see for comparison green and brown hysteresis loops in Fig. 6). Finally, in sample S1, when the number of structural defects within the NP is large enough, the hysteresis loops for all the cations in the two sublattices show features associated with the occurrence of strong canting.

5. CONCLUSIONS

We have investigated a series of samples of monodisperse Co-ferrite NP of 8 nm average size with similar stoichiometry and cation distribution but of tunable crystalline quality along the samples. SQUID magnetometry results show a rapid degradation of the collinear ferrimagnetism as structural disorder increases within the NP, and even samples that are almost free from crystallographic defects exhibit relatively large values of the high-field susceptibility suggesting the occurrence of canting at least for some of the cations and sites. Element-specific XAS and XMCD data reveal that the collinear alignment of Co^{2+} cations is much more affected by the structural disorder than that of the Fe^{3+} cations, the former showing a rapid increase of their canting even in NP containing only a few defects or crystallographic domain boundaries. This is because structural defects cause local distortions of the crystal field acting on the orbital component of the cations yielding effective local anisotropy axes that cause a prevalent Co^{2+} spin canting through the spin-orbit coupling, owing to the relatively large value of the partially unquenched moment of these cations, as found by XMCD. As the structural disorder is further increased, the rest of the cations in the two sublattices are progressively dragged off the ferrimagnetic alignment, being Fe^{3+}(Td) cations the last ones to be affected since the canting takes place firstly in Oh sites thanks to their smaller number of next-nearest neighbors in the Td-sublattice. Our results demonstrate the key role of the Co^{2+} cations on the destabilization of the collinear ferrimagnetism in Co-ferrite NP as their crystalline quality worsens and may help clarify the often conflicting, large variability of magnetic properties in the literature of Co-ferrite NP with slightly different structural features. This differentiates Co-ferrite from other ferrite NP that do not contain Co and, consequently, do not show such a great deterioration of the magnetic properties even for low-crystalline quality NP.

Our work may provide new avenues to interpret and control the functional response of Co-ferrite NP, of relevance in the fields of rare-earth free permanent magnets, biological separation and detection, or nanomedicine.

On a broader perspective, our results highlight the key importance of combining advanced synthesis techniques

enabling to prepare NP with a great control over the structural features with the use of complementary local probes with element, valence- and site- sensitivity so as to enhance the performance of nanoscale magnetic materials.

SUPPORTING INFORMATION

The Supporting Information is available free of charge at http://pubs.acs.org.

HAADF images and EDX maps; fits of the magnetization curves to Eq. (1); XMCD spectra calculated using ligand field multiplet theory for Fe and Co cations in Oh and Td sites; comparison of the XMCD hysteresis loops recorded in TEY and TFY modes for sample S4.

AUTHOR INFORMATION

Corresponding Author

* arantxa.fraile@ub.edu

Author Contributions

The manuscript was written through contributions of all authors. All authors have given approval to the final version of the manuscript.

Funding Sources

This work was supported by the Spanish MINECO projects MAT2015-68772-P and PGC2018-097789-B-I00 and European Union FEDER funds.

ACKNOWLEDGMENTS

M.E.T. acknowledges Spanish MINECO for the Ph.D. contract BES-2016-077527. A.F.R. and C.M acknowledge financial support from the EU CALIPSO Transnational Access programme. The general facilities of the University of Barcelona (CCiTUB) for the TEM, XRD and SQUID measurements, as well as the support with the measurements at FEI TITAN^3 of the Laboratorio de Microscopias Avanzadas (LMA) at Instituto de Nanociencia de Aragón (INA)-Universidad de Zaragoza, are also gratefully acknowledged. S.R.V.A. thanks the Swiss National Science Foundation for financial support under Project Nr. 169467.

ABBREVIATIONS

FC, field cooled; HRTEM, High-resolution TEM; HAADF, High-Angle Annular Dark-Field; EDX, Energy Dispersive X-ray spectroscopy; LFM, ligand field multiplet; NP, nanoparticle/s; Oh, octahedral; Td, tetrahedral; TEY, Total Electron Yield; TFY, Total Fluorescence Yield; TEM, Transmission Electron Microscopy; XAS, X-ray Absorption Spectroscopy; XMCD, X-ray Magnetic Circular Dichroism; ZFC, zero field cooled.

REFERENCES

(1) Srinivasan, S. Y.; Paknikar, K. M.; Bodas, D.; Gajbhiye, V. Applications of Cobalt Ferrite Nanoparticles in Biomedical Nanotechnology. *Nanomedicine*. Future Medicine Ltd. May 2018, pp 1221–1238. https://doi.org/10.2217/nnm-2017-0379.

(2) Amiri, S.; Shokrollahi, H. The Role of Cobalt Ferrite Magnetic Nanoparticles in Medical Science. *Materials Science and Engineering C*. Elsevier January 2013, pp 1–8. https://doi.org/10.1016/j.msec.2012.09.003.

(3) Wu, L.; Jubert, P. O.; Berman, D.; Imaino, W.; Nelson, A.; Zhu, H.; Zhang, S.; Sun, S. Monolayer Assembly of Ferrimagnetic $Co_xFe_{3-x}O_4$ Nanocubes for Magnetic Recording. *Nano Lett.* **2014**, *14* (6), 3395–3399. https://doi.org/10.1021/nl500904a.

(4) Cullity, B. D.; Graham, C. D. *Introduction to Magnetic Materials*; John Wiley & Sons, Inc.: Hoboken, NJ, USA, 2008. https://doi.org/10.1002/9780470386323.

(5) Sathya, A.; Guardia, P.; Brescia, R.; Silvestri, N.; Pugliese, G.; Nitti, S.; Manna, L.; Pellegrino, T. $Co_xFe_{3-x}O_4$ Nanocubes for Theranostic Applications: Effect of Cobalt Content and Particle Size. *Chem. Mater.* **2016**, *28* (6), 1769–1780. https://doi.org/10.1021/acs.chemmater.5b04780.

(6) Mohapatra, J.; Xing, M.; Liu, J. P. Magnetic and Hyperthermia Properties of $Co_xFe_{3-x}O_4$ Nanoparticles Synthesized via Cation Exchange. *AIP Adv.* **2018**, *8* (5), 056725. https://doi.org/10.1063/1.5006515.

(7) Rakshit, R.; Pal, M.; Chaudhuri, A.; Mandal, M.; Mandal, K. Research Update: Facile Synthesis of $CoFe_2O_4$ Nano-Hollow Spheres for Efficient Bilirubin Adsorption. *APL Mater.* **2015**, *3* (11), 110701. https://doi.org/10.1063/1.4935311.

(8) Bohara, R. A.; Throat, N. D.; Mulla, N. A.; Pawar, S. H. Surface-Modified Cobalt Ferrite Nanoparticles for Rapid Capture, Detection, and Removal of Pathogens: A Potential Material for Water Purification. *Appl. Biochem. Biotechnol.* **2017**, *182* (2), 598–608. https://doi.org/10.1007/s12010-016-2347-6.

(9) Abdolmohammad-Zadeh, H.; Rahimpour, E. $CoFe_2O_4$ Nano-Particles Functionalized with 8-Hydroxyquinoline for Dispersive Solid-Phase Micro-Extraction and Direct Fluorometric Monitoring of Aluminum in Human Serum and Water Samples. *Anal. Chim. Acta* **2015**, *881*, 54–64. https://doi.org/10.1016/j.aca.2015.04.035.

(10) Li, Y.; Zhang, Q.; Nurmikko, A. V.; Sun, S. Enhanced Magnetooptical Response in Dumbbell-like Ag-$CoFe_2O_4$ Nanoparticle Pairs. *Nano Lett.* **2005**, *5* (9), 1689–1692. https://doi.org/10.1021/nl050814j.

(11) Peddis, D.; Cannas, C.; Piccaluga, G.; Agostinelli, E.; Fiorani, D. Spin-Glass-like Freezing and Enhanced Magnetization in Ultra-Small $CoFe_2O_4$ Nanoparticles. *Nanotechnology* **2010**, *21* (12), 125705. https://doi.org/10.1088/0957-4484/21/12/125705.

(12) Song, Q.; Zhang, Z. J. Shape Control and Associated Magnetic Properties of Spinel Cobalt Ferrite Nanocrystals. *J. Am. Chem. Soc.* **2004**, *126* (19), 6164–6168. https://doi.org/10.1021/ja049931r.

(13) Moya, C.; Morales, M. D. P.; Batlle, X.; Labarta, A. Tuning the Magnetic Properties of Co-Ferrite Nanoparticles through the 1,2-Hexadecanediol Concentration in the Reaction Mixture. *Phys. Chem. Chem. Phys.* **2015**, *17* (19), 13143–13149. https://doi.org/10.1039/c5cp01052g.

(14) Moya, C.; Salas, G.; Morales, M. D. P.; Batlle, X.; Labarta, A. Inducing Glassy Magnetism in Co-Ferrite Nanoparticles through Crystalline Nanostructure. *J. Mater. Chem. C* **2015**, *3* (17), 4522–4529. https://doi.org/10.1039/c4tc02889a.

(15) Daffé, N.; Choueikani, F.; Neveu, S.; Arrio, M. A.; Juhin, A.; Ohresser, P.; Dupuis, V.; Sainctavit, P. Magnetic Anisotropies and Cationic Distribution in $CoFe_2O_4$ Nanoparticles Prepared by Co-Precipitation Route: Influence of Particle Size and Stoichiometry. *J. Magn. Magn. Mater.* **2018**, *460*, 243–252. https://doi.org/10.1016/j.jmmm.2018.03.041.

(16) Nappini, S.; Magnano, E.; Bondino, F.; Píš, I.; Barla, A.; Fantechi, E.; Pineider, F.; Sangregorio, C.; Vaccari, L.; Venturelli, L.; Baglioni, P. Surface Charge and Coating of $CoFe_2O_4$ Nanoparticles: Evidence of Preserved Magnetic and Electronic Properties. *J. Phys. Chem. C* **2015**, *119* (45), 25529–25541. https://doi.org/10.1021/acs.jpcc.5b04910.

(17) Bartolomé, E.; Cayado, P.; Solano, E.; Ricart, S.; Gázquez, J.; Mundet, B.; Coll, M.; Puig, T.; Obradors, X.; Valvidares, M.; Herrero-Martín, J.; Gargiani, P.; Pellegrin, E. Magnetic Stability against Calcining of Microwave-Synthesized $CoFe_2O_4$ Nanoparticles. *New J. Chem.* **2016**, *40* (8), 6890–6898. https://doi.org/10.1039/c6nj00705h.

(18) Moyer, J. A.; Vaz, C. A. F.; Arena, D. A.; Kumah, D.; Negusse, E.; Henrich, V. E. Magnetic Structure of Fe-Doped $CoFe_2O_4$ Probed by x-Ray Magnetic Spectroscopies. *Phys. Rev. B - Condens. Matter Mater. Phys.* **2011**, *84* (5), 1–10.

https://doi.org/10.1103/PhysRevB.84.054447.

(19) Moyer, J. A.; Vaz, C. A. F.; Kumah, D. P.; Arena, D. A.; Henrich, V. E. Enhanced Magnetic Moment in Ultrathin Fe-Doped $CoFe_2O_4$ Films. *Phys. Rev. B - Condens. Matter Mater. Phys.* **2012**, *86* (17), 1–8. https://doi.org/10.1103/PhysRevB.86.174404.

(20) Torres, T. E.; Lima, E.; Mayoral, A.; Ibarra, A.; Marquina, C.; Ibarra, M. R.; Goya, G. F. Validity of the Néel-Arrhenius Model for Highly Anisotropic $Co_xFe_{3-x}O_4$ Nanoparticles. *J. Appl. Phys.* **2015**, *118* (18). https://doi.org/10.1063/1.4935146.

(21) Tancredi, P.; Rivas-Rojas, P. C.; Moscoso-Londoño, O.; Muraca, D.; Knobel, M.; Socolovsky, L. M. Significant Coercivity Enhancement at Low Temperatures in Magnetically Oriented Cobalt Ferrite Nanoparticles. *Appl. Phys. Lett.* **2019**, *115* (26), 263104. https://doi.org/10.1063/1.5131259.

(22) Fantechi, E.; Campo, G.; Carta, D.; Corrias, A.; De Julián Fernández, C.; Gatteschi, D.; Innocenti, C.; Pineider, F.; Rugi, F.; Sangregorio, C. Exploring the Effect of Co Doping in Fine Maghemite Nanoparticles. *J. Phys. Chem. C* **2012**, *116* (14), 8261–8270. https://doi.org/10.1021/jp300806j.

(23) Gyergyek, S.; Makovec, D.; Kodre, A.; Arčon, I.; Jagodič, M.; Drofenik, M. Influence of Synthesis Method on Structural and Magnetic Properties of Cobalt Ferrite Nanoparticles. *J. Nanoparticle Res.* **2010**, *12* (4), 1263–1273. https://doi.org/10.1007/s11051-009-9833-5.

(24) Venturini, J.; Tonelli, A. M.; Wermuth, T. B.; Zampiva, R. Y. S.; Arcaro, S.; Da Cas Viegas, A.; Bergmann, C. P. Excess of Cations in the Sol-Gel Synthesis of Cobalt Ferrite ($CoFe_2O_4$): A Pathway to Switching the Inversion Degree of Spinels. *J. Magn. Magn. Mater.* **2019**, *482*, 1–8. https://doi.org/10.1016/j.jmmm.2019.03.057.

(25) Fantauzzi, M.; Secci, F.; Angotzi, M. S.; Passiu, C.; Cannas, C.; Rossi, A. Nanostructured Spinel Cobalt Ferrites: Fe and Co Chemical State, Cation Distribution and Size Effects by X-Ray Photoelectron Spectroscopy. *RSC Adv.* **2019**, *9*, 19171. https://doi.org/10.1039/c9ra03488a.

(26) Stohr, J.; Padmore, H. A.; Anders, S.; Stammler, T.; Scheinfein, M. R. Principles of X-Ray Magnetic Dichroism Spectromicroscopy. *Surf. Rev. Lett.* **1998**, *5* (6), 1297–1308.

(27) van der Laan, G.; Figueroa, A. I. X-Ray Magnetic Circular Dichroism - A Versatile Tool to Study Magnetism. *Coord. Chem. Rev.* **2014**, *277*, 95–129. https://doi.org/10.1016/j.ccr.2014.03.018.

(28) Fraile Rodríguez, A.; Moya, C.; Escoda-Torroella, M.; Romero, A.; Labarta, A.; Batlle, X. Probing the Variability in Oxidation States of Magnetite Nanoparticles by Single-Particle Spectroscopy. *J. Mater. Chem. C* **2018**, *6* (4), 875–882. https://doi.org/10.1039/c7tc03010j.

(29) Sun, S.; Zeng, H.; Robinson, D. B.; Raoux, S.; Rice, P. M.; Wang, S. X.; Li, G. Monodisperse MFe_2O_4 (M = Fe, Co, Mn) Nanoparticles. *J. Am. Chem. Soc.* **2004**, *126* (1), 273–279. https://doi.org/10.1021/ja0380852.

(30) Hyeon, T.; Su Seong Lee; Park, J.; Chung, Y.; Hyon Bin Na. Synthesis of Highly Crystalline and Monodisperse Maghemite Nanocrystallites without a Size-Selection Process. *J. Am. Chem. Soc.* **2001**, *123* (51), 12798–12801. https://doi.org/10.1021/ja016812s.

(31) Manna, L.; Scher, E. C.; Alivisatos, A. P. Synthesis of Soluble and Processable Rod-, Arrow-, Teardrop-, and Tetrapod-Shaped CdSe Nanocrystals. *J. Am. Chem. Soc.* **2000**, *122* (51), 12700–12706. https://doi.org/10.1021/ja003055+.

(32) Puntes, V. F.; Krishnan, K. M.; Alivisatos, A. P. Colloidal Nanocrystal Shape and Size Control: The Case of Cobalt. *Science (80-.).* **2001**, *291* (5511), 2115—2117. https://doi.org/10.1126/science.1057553.

(33) Reference Code 01-077-0426 Calculated from ICSD POWD-12++. 1997.

(34) Jensen, H.; Pedersen, J. H.; J∅rgensen, J. E.; Pedersen, J. S.; Joensen, K. D.; Iversen, S. B.; S∅gaard, E. G. Determination of Size Distributions in Nanosized Powders by TEM, XRD, and SAXS. *J. Exp. Nanosci.* **2006**, *1* (3), 355–373. https://doi.org/10.1080/17458080600752482.

(35) Bean, C. P.; Livingston, J. D. Superparamagnetism. *J. Appl. Phys.* **1959**, *30* (4), S120–S129. https://doi.org/10.1063/1.2185850.

(36) Piamonteze, C.; Flechsig, U.; Rusponi, S.; Dreiser, J.; Heidler, J.; Schmidt, M.; Wetter, R.; Calvi, M.; Schmidt, T.; Pruchova, H.; Krempasky, J.; Quitmann, C.; Brune, H.; Nolting, F. X-Treme Beamline at SLS: X-Ray Magnetic Circular and Linear Dichroism at High Field and Low Temperature. *J. Synchrotron Radiat.* **2012**, *19* (5), 661–674. https://doi.org/10.1107/S0909049512027847.

(37) Peddis, D.; Orrù, F.; Ardu, A.; Cannas, C.; Musinu, A.; Piccaluga, G. Interparticle Interactions and Magnetic Anisotropy in Cobalt Ferrite Nanoparticles: Influence of Molecular Coating. *Chem. Mater.* **2012**, *24* (6), 1062–1071. https://doi.org/10.1021/cm203280y.

(38) Torres, T. E.; Roca, A. G.; Morales, M. P.; Ibarra, A.; Marquina, C.; Ibarra, M. R.; Goya, G. F. Magnetic Properties and Energy Absorption of $CoFe_2O_4$ Nanoparticles for Magnetic Hyperthermia. *J. Phys. Conf. Ser.* **2010**, *200* (SECTION 7). https://doi.org/10.1088/1742-6596/200/7/072101.

(39) Cabrera, L. I.; Somoza, Á.; Marco, J. F.; Serna, C. J.; Puerto Morales, M. Synthesis and Surface Modification of Uniform MFe_2O_4 (M = Fe, Mn, and Co) Nanoparticles with Tunable Sizes and Functionalities. *J. Nanoparticle Res.* **2012**, *14* (6). https://doi.org/10.1007/s11051-012-0873-x.

(40) Bao, N.; Shen, L.; Wang, Y.; Padhan, P.; Gupta, A. A Facile Thermolysis Route to Monodisperse Ferrite Nanocrystals. *J. Am. Chem. Soc.* **2007**, *129* (41), 12374–12375. https://doi.org/10.1021/ja074458d.

(41) Mahhouti, Z.; El Moussaoui, H.; Mahfoud, T.; Hamedoun, M.; El Marssi, M.; Lahmar, A.; El Kenz, A.; Benyoussef, A. Chemical Synthesis and Magnetic Properties of Monodisperse Cobalt Ferrite Nanoparticles. *J. Mater. Sci. Mater. Electron.* **2019**, *30* (16), 14913–14922. https://doi.org/10.1007/s10854-019-01863-3.

(42) Baaziz, W.; Pichon, B. P.; Liu, Y.; Grenèche, J. M.; Ulhaq-Bouillet, C.; Terrier, E.; Bergeard, N.; Halté, V.; Boeglin, C.; Choueikani, F.; Toumi, M.; Mhiri, T.; Begin-Colin, S. Tuning of Synthesis Conditions by Thermal Decomposition toward Core-Shell $Co_xFe_{1-x}O@Co_yFe_{3-y}O_4$ and $CoFe_2O_4$ Nanoparticles with Spherical and Cubic Shapes. *Chem. Mater.* **2014**, *26* (17), 5063–5073. https://doi.org/10.1021/cm502269s.

(43) Abdulwahab, K. O.; Malik, M. A.; O'Brien, P.; Timco, G. A.; Tuna, F.; Muryn, C. A.; Winpenny, R. E. P.; Pattrick, R. A. D.; Coker, V. S.; Arenholz, E. A One-Pot Synthesis of Monodispersed Iron Cobalt Oxide and Iron Manganese Oxide Nanoparticles from Bimetallic Pivalate Clusters. *Chem. Mater.* **2014**, *26* (2), 999–1013. https://doi.org/10.1021/cm403047v.

(44) Coker, V. S.; Pearce, C. I.; Pattrick, R. A. D.; Van Der Laan, G.; Telling, N. D.; Charnock, J. M.; Arenholz, E.; LLoyd, J. R. Probing the Site Occupancies of Co-,Ni-, and Mn-Substituted Biogenic Magnetite Using XAS and XMCD. *Am. Mineral.* **2008**, *93* (7), 1119–1132. https://doi.org/10.2138/am.2008.2681.

(45) Carvallo, C.; Sainctavit, P.; Arrio, M. A.; Menguy, N.; Wang, Y.; Ona-Nguema, G.; Brice-Profeta, S. Biogenic vs. Abiogenic Magnetite Nanoparticles: A XMCD Study. *Am. Mineral.* **2008**, *93* (5–6), 880–885. https://doi.org/10.2138/am.2008.2713.

(46) Coker, V. S.; Telling, N. D.; Van Der Laan, G.; Pattrick, R. A. D.; Pearce, C. I.; Arenholz, E.; Tuna, F.; Winpenny, R. E. P.; Lloyd, J. R. Harnessing the Extracellular Bacterial Production of Nanoscale Cobalt Ferrite with Exploitable Magnetic Properties. *ACS Nano* **2009**, *3* (7), 1922–1928. https://doi.org/10.1021/nn900293d.

(47) Van Der Laan, G.; Thole, B. T. Strong Magnetic X-Ray Dichroism in 2p Absorption Spectra of 3d Transition-Metal Ions. *Phys. Rev. B* **1991**, *43* (16), 13401–13411. https://doi.org/10.1103/PhysRevB.43.13401.

(48) Van Der Laan, G.; Kirkman, I. W. The 2p Absorption Spectra of 3d Transition Metal Compounds in Tetrahedral and Octahedral Symmetry. *J. Phys. Condens. Matter* **1992**, *4* (16), 4189–4204. https://doi.org/10.1088/0953-8984/4/16/019.

(49) Stavitski, E.; de Groot, F. M. F. The CTM4XAS Program for EELS and XAS Spectral Shape Analysis of Transition Metal L Edges. *Micron* **2010**, *41* (7), 687–694. https://doi.org/10.1016/j.micron.2010.06.005.

(50) Pearce, C. I.; Henderson, C. M. B.; Pattrick, R. A. D.; van der

Laan, G.; Vaughan, D. J. Direct Determination of Cation Site Occupancies in Natural Ferrite Spinels by $L_{2,3}$ X-Ray Absorption Spectroscopy and X-Ray Magnetic Circular Dichroism. *Am. Mineral.* **2006**, *91* (5–6), 880–893. https://doi.org/10.2138/am.2006.2048.

(51) Thole, B. T.; Carra, P.; Sette, F.; Van Der Laan, G. X-Ray Circular Dichroism as a Probe of Orbital Magnetization. *Phys. Rev. Lett.* **1992**, *68* (12), 1943–1946. https://doi.org/10.1103/PhysRevLett.68.1943.

(52) Carra, P.; Thole, B. T.; Altarelli, M.; Wang, X. X-Ray Circular Dichroism and Local Magnetic Fields. *Phys. Rev. Lett.* **1993**, *70* (5), 694–697. https://doi.org/10.1103/PhysRevLett.70.694.

(53) Chen, C. T.; Idzerda, Y. U.; Lin, H. J.; Smith, N. V.; Meigs, G.; Chaban, E.; Ho, G. H.; Pellegrin, E.; Sette, F. Experimental Confirmation of the X-Ray Magnetic Circular Dichroism Sum Rules for Iron and Cobalt. *Phys. Rev. Lett.* **1995**, *75* (1), 152–155. https://doi.org/10.1103/PhysRevLett.75.152.

(54) Van Der Laan, G.; Arenholz, E.; Chopdekar, R. V.; Suzuki, Y. Influence of Crystal Field on Anisotropic X-Ray Magnetic Linear Dichroism at the Co^{2+} $L_{2,3}$ Edges. *Phys. Rev. B - Condens. Matter Mater. Phys.* **2008**, *77* (6), 1–11. https://doi.org/10.1103/PhysRevB.77.064407.

(55) Pérez, N.; Bartolomé, F.; García, L. M.; Bartolomé, J.; Morales, M. P.; Serna, C. J.; Labarta, A.; Batlle, X. Nanostructural Origin of the Spin and Orbital Contribution to the Magnetic Moment in $Fe_{3-x}O_4$ Magnetite Nanoparticles. *Appl. Phys. Lett.* **2009**, *94* (9), 4–7. https://doi.org/10.1063/1.3095484.

(56) Batlle, X.; Pérez, N.; Guardia, P.; Iglesias, O.; Labarta, A.; Bartolomé, F.; Garca, L. M.; Bartolomé, J.; Roca, A. G.; Morales, M. P.; Serna, C. J. Magnetic Nanoparticles with Bulklike Properties (Invited). *J. Appl. Phys.* **2011**, *109* (7), 1–6. https://doi.org/10.1063/1.3559504.

(57) Slick, P. I. Ferrites for Non-Microwave Applications. In *Ferromagnetic materials: A Handbook on the Properties of Magnetically Ordered Substances*; Wohlfarth, E. P., Ed.; North-Holland Publishing Company: Amsterdam, 1980; Vol. 2, p 189.

(58) Srivastava, C. M.; Srinivasan, G.; Nanadikar, N. G. Exchange Constants in Spinel Ferrites. *Phys. Rev. B* **1979**, *19* (1), 499–508. https://doi.org/10.1103/PhysRevB.19.499.

(59) Ouaissa, S.; Benyoussef, A.; Abo, G. S.; Ouaissa, M.; Hafid, M. Magnetization Study of Cobalt Ferrite by Mean Field Approximation. *Phys. Procedia* **2015**, *75*, 792–801. https://doi.org/10.1016/j.phpro.2015.12.103.

(60) Yu, Y.; Mendoza-Garcia, A.; Ning, B.; Sun, S. Cobalt-Substituted Magnetite Nanoparticles and Their Assembly into Ferrimagnetic Nanoparticle Arrays. *Adv. Mater.* **2013**, *25* (22), 3090–3094. https://doi.org/10.1002/adma.201300595.

(61) Hu, G.; Choi, J.; Eom, C.; Harris, V.; Suzuki, Y. Structural Tuning of the Magnetic Behavior in Spinel-Structure Ferrite Thin Films. *Phys. Rev. B - Condens. Matter Mater. Phys.* **2000**, *62* (2), R779–R782. https://doi.org/10.1103/PhysRevB.62.R779.

(62) Moyer, J. A.; Vaz, C. A. F.; Negusse, E.; Arena, D. A.; Henrich, V. E. Controlling the Electronic Structure of $Co_{1-x}Fe_{2+x}O_4$ Thin Films through Iron Doping. *Phys. Rev. B - Condens. Matter Mater. Phys.* **2011**, *83* (3), 1–10. https://doi.org/10.1103/PhysRevB.83.035121.

(63) Peddis, D.; Yaacoub, N.; Ferretti, M.; Martinelli, A.; Piccaluga, G.; Musinu, A.; Cannas, C.; Navarra, G.; Greneche, J. M.; Fiorani, D. Cationic Distribution and Spin Canting in $CoFe_2O_4$ Nanoparticles. *J. Phys. Condens. Matter* **2011**, *23* (42). https://doi.org/10.1088/0953-8984/23/42/426004.

(64) Sawatzky, G. A.; Van Der Woude, F.; Morrish, A. H. Mössbauer Study of Several Ferrimagnetic Spinels. *Phys. Rev.* **1969**, *187* (2), 747–757. https://doi.org/10.1103/PhysRev.187.747.

(65) Standley, K. J. *Oxide Magnetic Materials*; Clarendon Press, 1972.

For Table of Contents Use Only